First measurements with the Faraday cup fast ion loss detector on Wendelstein 7-X

Samuel A. Lazerson ✉ ⓘ ; David J. Kulla ⓘ ; Alexandra LeViness ⓘ ; Brandon F. Lee ⓘ ; Matthias Steffen; Beate Kursinski; Karsten Ewert; the W7-X Team

Check for updates

View Online   Export Citation

Articles You May Be Interested In

Simulation of a scintillator-based fast ion loss detector for steady-state operation in Wendelstein 7-X (invited)

Rev. Sci. Instrum. (July 2024)

OPTEMIST: A neutral beam for measuring quasi-omnigenity in Wendelstein 7-X

Phys. Plasmas (July 2024)

Comparative collisionless alpha particle confinement in stellarator reactors with the XGC gyrokinetic code

Phys. Plasmas (March 2019)

AIP Publishing

First measurements with the Faraday cup fast ion loss detector on Wendelstein 7-X

View Online   Export Citation   CrossMark

Samuel A. Lazerson,[1,a] (ID) David J. Kulla,[2] (ID) Alexandra LeViness,[3] (ID) Brandon F. Lee,[3] (ID) Matthias Steffen,[4]
Beate Kursinski,[4] Karsten Ewert,[4] and the W7-X Team[b]

AFFILIATIONS

[1] Gauss Fusion GmbH, Garching bei München 85748, Germany
[2] Max-Planck-Institut für Plasmaphysik, Garching bei München 85748, Germany
[3] Princeton University, Princeton, New Jersey 08544, USA
[4] Max-Planck-Institut für Plasmaphysik, Greifswald 17491, Germany

[a] Author to whom correspondence should be addressed: samuel.lazerson@gauss-fusion.com
[b] See author list of O. Grulke *et al.*, Nucl. Fusion **64**, 112002 (2024).

ABSTRACT

The first measurements made with a prototype Faraday cup fast ion loss detector (FC-FILD) on the Wendelstein 7-X (W7-X) device are presented and shown to be consistent with lost neutral beam fast ions. The FC-FILD is a small form factor, energy resolving detector designed to be mounted inside the first wall armor tiles of W7-X. Such mounting will allow for a future detector array to be installed, which has been shown to be critical for demonstrating improved fast ion confinement with plasma beta ($\beta = 2\mu_0 p/B^2$). The prototype diagnostic is composed of a movable armature with a water cooled diagnostic head, mimicking the first wall armor tile cooling structure. The movement of the armature allows for assessment of different detector positions relative to the plasma edge. Measurements of lost fast ions in the low shear magnetic configuration are correlated with neutral beam blips and the neutral beam energy spectrum. Analysis of the rise time of the signals presents a timescale much faster than the energy or particle confinement time and of the order of the predicted neutral beam fast ion slowing down time. Simulations predict a larger signal amplitude than measured, and possible reasons for this are discussed. Finally, a redesigned aperture is presented, which allows for fast ions to reach the detector in a larger set of magnetic configurations.

I. INTRODUCTION

The measurement of non-thermal ion losses in magnetically confined fusion devices has traditionally been performed using scintillator type fast ion loss detectors (FILDs).[1–6] These detectors provide measurements of both the pitch angle ($\cos \alpha = v_\parallel/v$) and energy of unconfined energetic ions using scintillating plates, Faraday screens, and camera systems. Fast ion deuterium-alpha (FIDA) and neutral particle analyzers (NPAs) provide a means of directly probing the fast ion distribution function but suffer at high densities and are limited by the neutral beam geometry. The size of these systems limits the number of such detectors, which can be implemented on a device. In three-dimensional systems such as the Wendelstein 7-X (W7-X) stellarator,[7] the loss pattern can change, necessitating a multi-point measurement system to properly discriminate changes in the fast ion load pattern from changes in overall confinement.[8]

Moreover, many of the places where one would like to make such measurements are not accessible for traditional detectors requiring a port. In addition, scintillator type detectors suffer from a poor signal in high temperature and neutron rich environments, making them of limited utility to study future fusion power plants, where both high temperatures and large neutron loads are expected.[9,10] To address these needs, the Faraday cup FILD (FC-FILD) sensor has been developed and has begun testing in the W7-X device.[11,12]

The FC-FILD sensor is an energy resolving sensor designed to fit inside the existing wall structure of magnetically confined fusion devices. The sensors themselves are small metal substrates ($39 \times 24 \times 2$ mm^3) upon which layers of insulating and conductive metals are deposited.[12] Energetic ions that are incident upon the sensor will penetrate the layer stack, with their ultimate depth being a function of their energy and angle of incidence. In this way, each conductive layer integrates charges over a given energy band, which is a
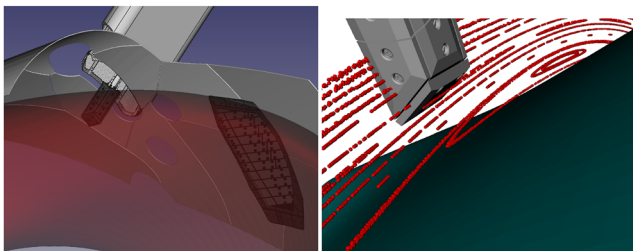
function of the layer's thickness. Thin layer deposition techniques are employed allowing for sub-micrometer layer thicknesses, which, in turn, allow measurement of energetic protons in the few tens of keV range, a challenge to measure with traditional FILD aperture designs.[13] The energy resolution of the sensors is a design parameter based on the channel number and layer thickness. The small size of these sensors allows for an "in-wall-tile" packaging concept, wherein individual wall tiles in an experiment can be instrumented. In addition, they are well suited for future nuclear fusion device environments (such as ITER), as their signal is unaffected by neutrons (and gamma rays) by design and can tolerate high temperature operation. In this work, aluminum and aluminum oxide are used, which only begin to become amorphous at around 700 °C.

As a demonstration and prototyping activity, one such sensor has been installed on a movable armature in the W7-X device (Fig. 1). The head of the armature was designed to mimic the thermal and packaging environment of a first wall armor tile on W7-X. In W7-X, the first wall armor is composed of graphite tiles bolted to CuCrZr heat sinks, which are brazed to stainless steel water cooling pipes. The armature head is a stainless steel structure with integrated water cooling channels. The plasma facing end of the armature also has a CuCrZr heat sink structure, an FC-FILD sensor, and a graphite tile. A small protrusion of the stainless steel head contains a water cooling channel, while the CuCrZr block contains a recess into which the protrusion fits. This feature attempts to mimic the water pipe heat-sink interface of the first wall. Movement of the manipulator allows different plasma wall distances to be evaluated and avoids possible contact with the scrape-off layer for different magnetic configurations.

In this work, we present the first measurements of escaping fast ions as measured using a prototype FC-FILD diagnostic in W7-X. In Sec. II, we describe the prototype designed to mimic the installation environment of a wall tile. In Sec. III, we document the measurement of lost neutral beam injected ions, and in Sec. IV, we conclude the work with an overview and future work. Detailed discussions of fast ion confinement in W7-X are covered in previous studies.[8,14–22]
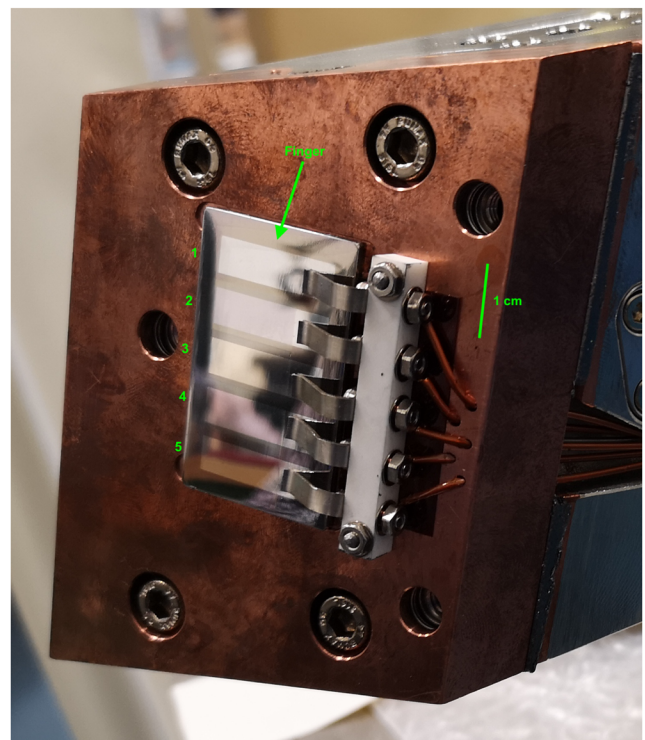
II. DESIGN

The prototype sensor for W7-X has gone through a series of design changes over its development to improve manufacturability

and operation. The fundamental concept of the sensor was demonstrated using thin foils to measure losses of highly energetic alpha particles (0.7–7 MeV) in the JET tokamak.[1] The high energy of these particles allowed the use of micrometer thick films as opposed to the sub-micrometer thick layers needed for measuring keV particles. The next iteration of the sensor used thin film deposition techniques to create a sandwich of sub-micrometer alternating layers of conductor and insulator.[11] While demonstrated in a linear tunable beam line, their manufacture proved to be difficult. This led to the current version installed on W7-X, which uses conducting aluminum fingers covered by differing thickness layers of aluminum oxide[12] (Fig. 2). This change simplified the manufacturing process while removing the possibility of shorting between channels. Electrical contact is made in regions where no Al_2O_3 overlay is present. An Al_2O_3 layer between the finger and substrate provides electrical isolation of the fingers from the rest of the structure.

Selection of the Al_2O_3 layer thickness was informed by simulations with the Stopping and Range of Ions in Matter (SRIM) code.[23] In Fig. 3, the sensor response for a variety of layer thicknesses and proton energies are shown. The thicknesses used for manufacture of the sensor are labeled. These choices of layer thickness attempt to capture the full, half, and third energy populations generated by the 55 kV neutral beam system on W7-X. With this choice,


FIG. 1. Rendering of the diagnostic head relative to the NBI beam duct (left) and relative to the last closed flux surface (right). In the figure on the left, the last closed magnetic surface of the standard magnetic configuration is depicted in red with the neutral beam port depicted in dark gray. In the figure on the right, the green surface depicts the plasma last closed flux surface with a vacuum Poincaré plot of the low shear magnetic configuration depicting the edge island chain.

FIG. 2. FC-FILD sensor with finger configuration installed on the prototype diagnostic head. The carbon armor has been removed showing the sensor mounted onto the CuCrZr heat sink with electrical contacts installed. The sensor channels are numbered, with slight differences in the finger color being attributed to differences in the Al_2O_3 thickness. The white bus bar is Al_2O_3, and the wires are insulated with Kapton.
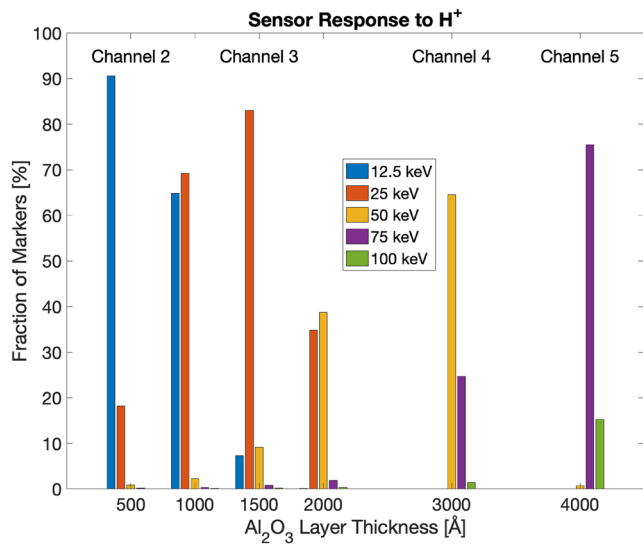
FIG. 3. FC-FILD sensor response to different energetic ion populations as a function of insulating Al_2O_3 layer thickness. Channel names reference channels of the installed sensor on W7-X. Fractions in terms of total incident particles onto the sensor. The calculations are performed with the SRIM code.[23]
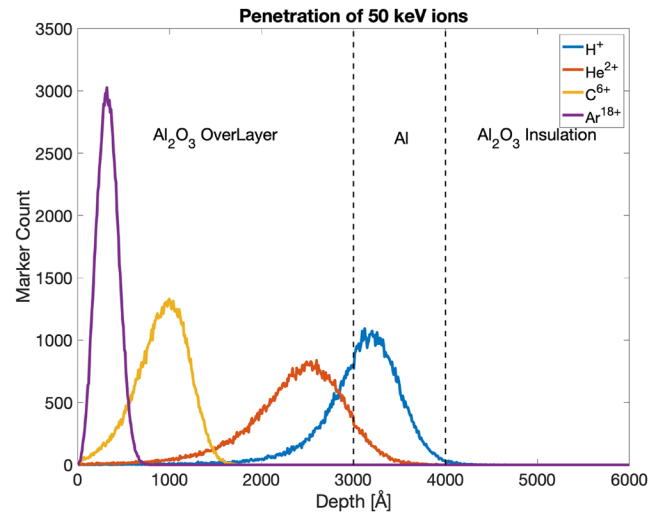
FIG. 4. Histogram of particle depths for a 3000 Å Al_2O_3 insulating layer exploring different ions at a fixed 50 keV incident energy. Note that the core ion temperature in W7-X is rarely above 1.5 keV. In each case, 100 000 markers were injected.

channel 5 serves two purposes. First, it provides a control as one would not expect a signal in channel 5 during NBI operation. Second, W7-X plans to use ion cyclotron resonance heating both in a three-ion scheme and along with NBI to produce particles with energies above the W7-X NBI energies.[24] The plot shows fractions of incident particles for each layer thickness. Thus, for any given incident energy, between 60% and 70% of the particles are captured in their respective finger.

Simulation such as these take into account the large pitch angle scattering collisions that occur with the Al nuclei along with purely slowing down collisions due to the electron clouds surrounding the Al atoms. In the case of an insulating layer covering the Al sensing layer, it is assumed that the stopping of ions in the metal translates to signal. In a previous study, this was confirmed, as the total current measured in the sensing layer agreed well with the measured beam line current.[11] However, in that work, an additional top conducting layer was also present. The top exposed layer indicated a measured current two to three times higher than the beam current (~200 nA vs ~80 nA in the beam line). Secondary electron emission and the possibility of the formation of a local plasma sheath were proposed as mechanisms for this signal.

The penetration of impurity ions into the material for a given energy would be much smaller than that for incident protons. As the atomic number of the material, incident ion, or both goes up, the role scattering collisions play also goes up. Simulations show that for heavier material targets than Al_2O_3 (and Al), the penetration depth at a given energy decreases. However, the transverse motion (perpendicular to the angle of incidence) increases. The same holds for heavier ions impinging into the existing sensor (Fig. 4). Thus, we expect impurity ions to play a role only if accelerated to very large velocities.

The prototype FC-FILD sensor on W7-X is mounted on a movable manipulator, which mimics an in-wall tile mounting setup (Fig. 5). The diagnostic head is composed of a stainless steel water cooled block cladded with protective carbon tiles. The stainless steel block was manufactured using selective laser melting. This allowed water channels that both cool the system and mimic the water channel–wall tile interface in W7-X. The sensor is mounted on a CuCrZr block designed to mimic the heat-sink and water pipe system of the W7-X first wall. A carbon tile with a 40×5 mm^2 aperture provides a path by which particles can reach the sensor fingers. A support and bellows system allows the head to be pneumatically actuated from outside the vacuum vessel. This allows the diagnostic head to retract slightly behind the steel wall panels and insert by 25 cm toward the plasma. The insertion and retraction mechanism is controlled using a pneumatic actuator and helper spring. Insertion depth is controlled using a stepper motor actuated stopping plate. A custom logarithm amplifier converts sensor current to voltages, which are then digitized at 1 kHz. The overall control and data acquisition is performed using a LabJack T6-Pro. A thermocouple is located inside the CuCrZr block to monitor the detector head temperature.

The data acquisition system and logarithmic amplifier were calibrated using a Keithley 6221 AC and DC current source (Fig. 6). The source current was scanned from 1 nA to 100 mA, and the measured voltage was recorded for all channels. A logarithmic function for the voltage was fit to the data $V_{out} = \log_{10}(I/I_{min}) + V_{offset}$, where V_{out} is the measured voltage, I is the source current, I_{min} is the minimum current fit parameter, and V_{offset} is the offset voltage fit parameter. The fit to data for all channels was very good with similar behaviors for each channel. Only the 100 mA data point appears to be slightly off the curve. This is attributed to it being both the upper limit of the current source and the design upper limit of the amplifier itself. Noise with a frequency of 50 Hz and an amplitude of 0.5 nA was present in the 1 and 10 nA steps (a measured signal level of 2 nA

04 March 2025 08:16:00
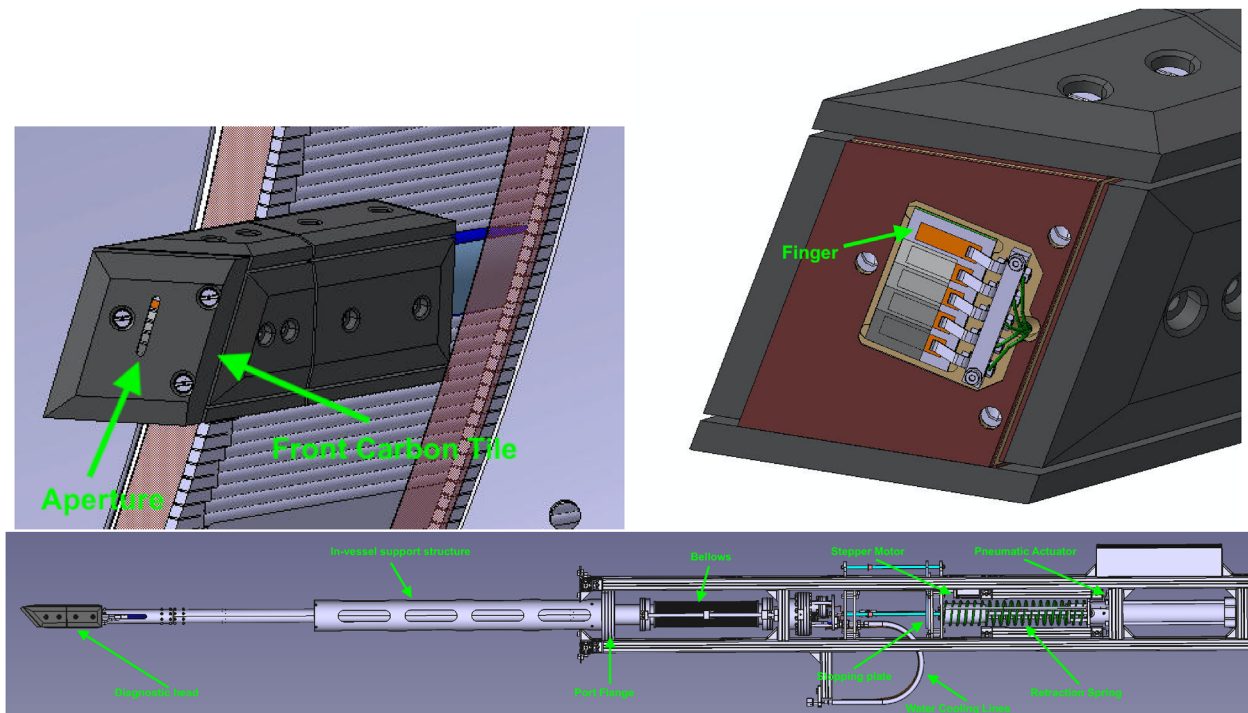
FIG. 5. Diagnostic overview showing the inserted diagnostic head (upper left), sensor behind the front carbon tile (upper right), and entire diagnostic with support and actuation structure (bottom). Various components of the diagnostic have been labeled.

will be shown in Sec. III). In these calibrations, current was applied to one channel, while measurements were made on all channels to detect cross coupling. No such coupling was detected. Capacitive coupling between fingers is expected to be very small given the finger layout. Postmortem tests showed that all channels maintained electrical isolation from each other and ground.

III. MEASUREMENT

The diagnostic and in-tile mounting concept proved itself over the course of a W7-X experimental campaign. The probe head was regularly inserted to the full depth with detector head temperatures staying well below 100 °C. In most configurations, this placed the
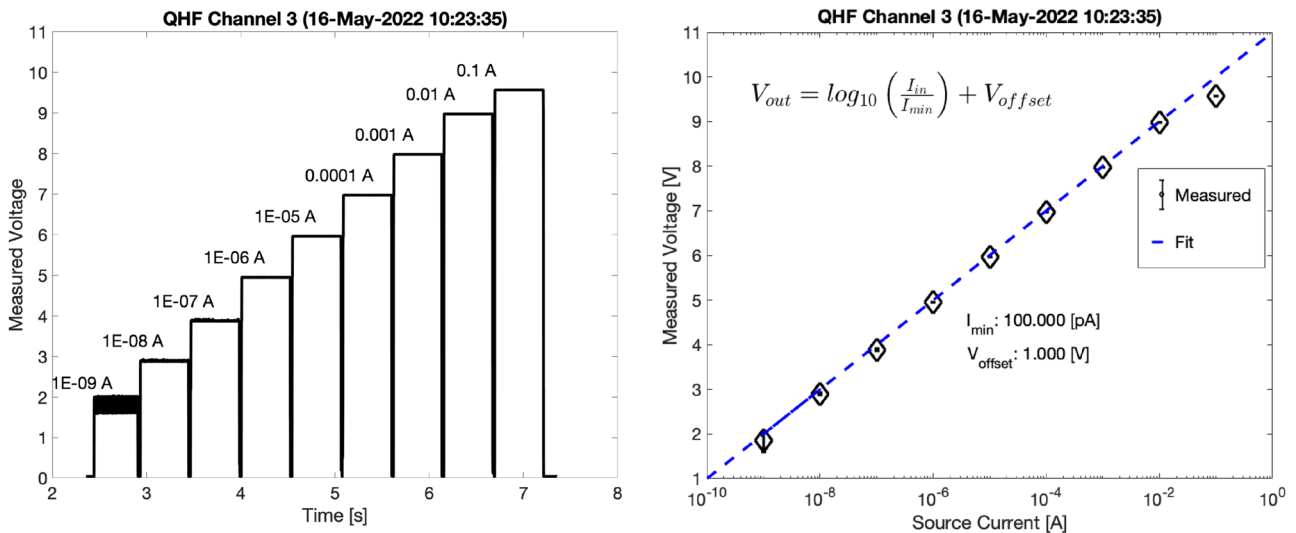
FIG. 6. Calibration data (left) and fit curve (right) for channel 3 of the diagnostic data acquisition system indicating a well calibrated system.

detector close to the plasma but still outside the edge island scrape-off-layer. A discharge with over 1 GJ of injected energy from electron cyclotron resonance heating (ECRH) was conducted, and the detector saw no concerning temperature rises. Unfortunately, the slit style aperture proved too restricting to allow measurement of any fast ion signals in most magnetic configurations. However, the outward shifted low shear magnetic configurations did allow for some fast ions to reach the sensor.

The neutral beam system on W7-X injects 55 keV hydrogen beams. This results in three distinct energy populations at the full, half, and third energy components. The power fractions for these three components are ~49 %, ~41 %, and ~10 %,[26] which give particle fractions of ~31 %, ~50 %, and ~19 %, respectively. Figure 7 depicts BEAMS3D simulations of the neutral beam deposition and global losses for the three energy components of source 7.[25,27] Despite the beam deposition being biased toward the half energy, the losses for the full and half energy components are similar. From this, the expectation is for signal levels in channels 4 and 3 to be of similar levels. However, this is based on global losses, while the FC-FILD is positioned at one point in space.

Figure 8 depicts the co-averaged measured signal for the five channels of the FC-FILD in the outward shifted low shear magnetic configuration. In this discharge, the neutral beam source S7 is pulsed at a frequency of 5 Hz (50% duty cycle) into a 4 MW ECRH plasma, while neutral beam source S4 was fired continuously. This periodic modulation of the beam is referred to as blipping of the beam in this text. Source 7 fires in the direction of the magnetic field and in the same field period as the sensor. Source 4 fires from a beam line in the neighboring field period but anti-parallel to the toroidal magnetic field. The plasma core electron density and temperature were 3.5×10^{19} m^{-3} and 3.0 keV, respectively. Spectroscopy of the neutral beam system places most of the power (neutral particles) in the 55 and 27.5 keV populations with only a small amount of the beam in the 18.3 kV population. Signal levels in the FC-FILD follow this
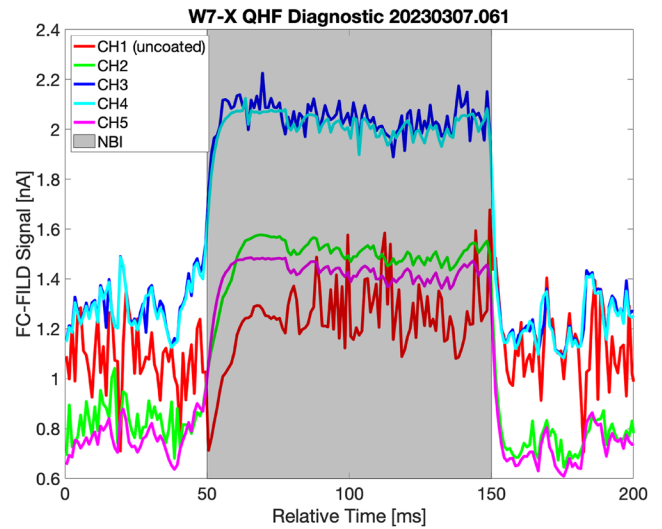
FIG. 8. Signal of the Faraday cup fast ion loss detector during a neutral beam blip. The signal is co-averaged over five NBI blips lasting 100 ms each. The shaded region shows the timing of the neutral beam blip.

trend with channel 3 (25 kV) and channel 4 (50 kV) having similar levels of signal and with channel 2 (12 keV) being subdominant. We note that the core ion temperature in this discharge was measured to be ~1.5 keV, much too low to be detectable in channels 2 through 5.

Examination of the raw signals during NBI blips suggests that the signal present in channel 1 is a combination of noise due to the plasma and electronics (Fig. 9). Here, we note that between blips of the NBI, there is a clear noise signal that decreases in amplitude when the beam fires. A small 50 Hz oscillation can be seen in channel 1 while the beam is firing. This is most likely some form of electronic
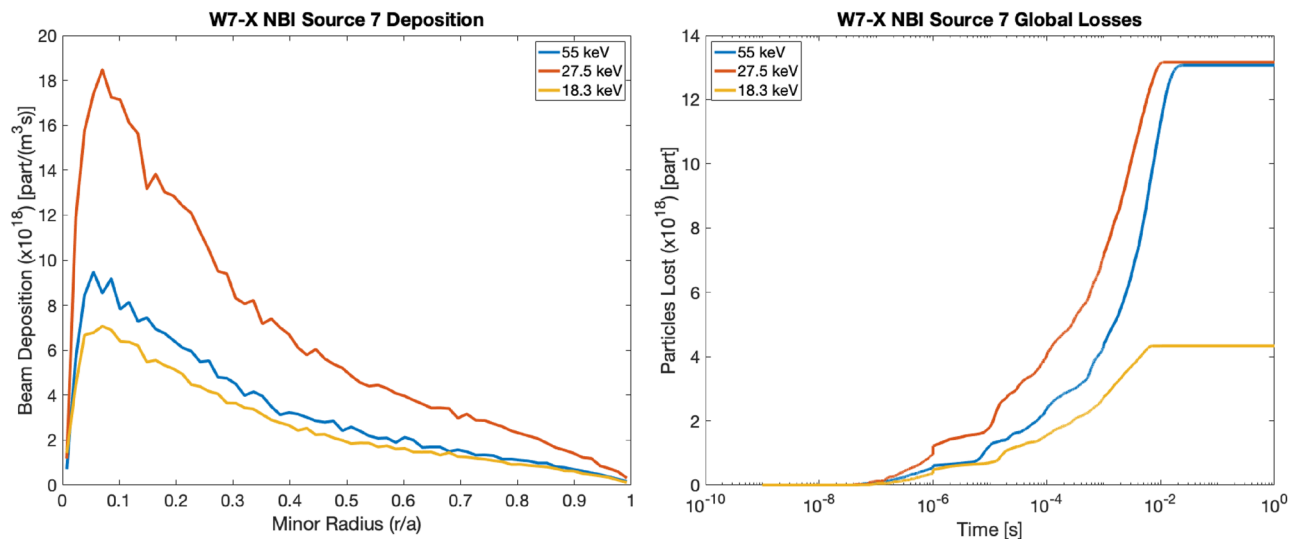
FIG. 7. Neutral beam deposition profile (left) and loss (right) data for W7-X NBI source 7 as simulated by the BEAMS3D code.[25]

04 March 2025 08:16:00
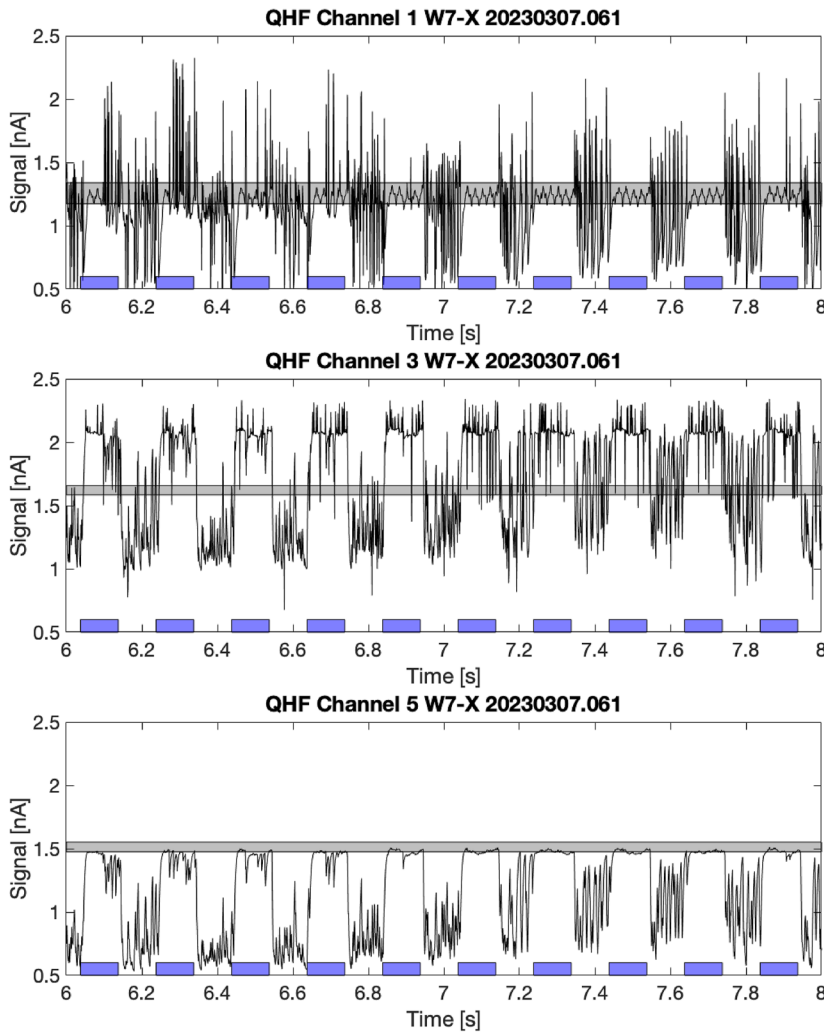
FIG. 9. Current traces for FC-FILD channels 1 (top), 3 (middle), and 5 (bottom) showing the behavior without coaveraging. A shaded region on the bottom of the plots has been added to indicate when source 7 was firing. A shaded region going across the plot indicates signal levels and noise amplitude before the discharge.

noise, as data taken before the discharge show a similar feature. It should be noted that the amplitude of this oscillation is much smaller than the 50 Hz oscillation seen during calibration. The other channels show a ~17 *Hz* square wave like feature in the signal before the plasma discharge, which disappears once the plasma is ignited. This 50 Hz signal is of the order of 50 pA in amplitude, much smaller than the measured response due to the neutral beam. For channels 2 through 5, the signal was well correlated with the neutral beam blips. It should also be noted that while source 7 is firing channel one sees an initial decrease in the signal and then a return to the signal level similar to that between NBI discharges. This effect can also be seen in Fig. 8.

The signal seen in channel 5 clearly correlates with the turning on and off of the neutral beam. However, one would not expect to see the signal in channel 5 from escaping fast ions or fast neutrals given the beam injection energy and plasmas parameters. Non-perpendicular incidence of particles onto the detectors results in the particle seeing an effective Al_2O_3 layer thickness, which is greater than that over the finger. Thus, such an effect can only result in a decrease in the measured energy of a particle and cannot explain why a higher energy signal would be present. In addition, destructive tests of another sample from this batch of depositions would suggest that the layer is thicker than the design value not thinner.[12] Assuming the measurement to be true, the data would suggest a layer that is thinner than the design parameter.

Looking at the period before the plasma is ignited, one finds a baseline value of 1.25, 1.6, 1.6, 1.5, and 1.5 nA in each channel (1–5), respectively. Using this offset as a basis, one would conclude that only the signal in channels 3 and 4 is significant (Fig. 8). Using the period between pulses of S7 as an offset, one finds that channels 3 and 4 still have the largest signal with channels 2 and 5 having similar amplitudes. Clearly, interpretation of these signals in absolute numbers requires additional calibration, as could be provided in a tunable beam line.

The question of coupling to the plasma is raised by the fact that the noise in the signals itself seems well correlated between channels.

The pure ECRH phase of the plasma shows a strong correlation with signals between channels. This is presumably due to some coupling mechanism between the plasma and the detector itself. Supporting this hypothesis is a drop in the signal for all channels as the plasma is ignited with ECRH by ~120 mV (1 nA as calibrated). In addition, the dominant frequency of the noise goes from ~17 Hz to something of the order of a few hundred Hz. While our signals show a correlation with the neutral beam discharges, one would like to eliminate the possibility that these signals could be attributed to changes in the plasma itself. This can be achieved by comparing signal timescales to the timescales associated with changes in temperature and density.

The rise time of the signals for the neutral beam blips can be compared to simulation data to give additional confidence that we are, in fact, measuring lost fast ions. In Fig. 10, the fit of the formula $f(t, a, b, c, d) = ae^{-(t-b)/c} + d$ to a single pulse of source 7 for channel 4 is depicted. Here, the parameter c is of interest as it is a characteristic time we can compare between the experiment and simulations. Gyrocenter simulations with the BEAMS3D code[18,25,27] find a value of 3.83 ms for the S7 source and plasma parameters similar to those of this discharge. Table I shows the fit parameters for each channel for a single blip of source 7. All channels find fit parameters that agree with the simulation value. A similar analysis of the diamagnetic energy gives a value for c of 14.8 ms, and the line integrated density shows a value of 131 ms. This gives confidence to the notion that the detector is measuring lost fast ions and not simply seeing the effect of changes in plasma parameters.

Electromagnetic pickup can also be ruled out as a source of the signal. The measurement period of the sensor covers slightly before plasma startup and during the phase before the NBI is fired, and no significant signal is seen. Electromagnetic pickup from the NBI itself can also be ruled out, as measurement is made during tests of the NBI into the empty torus, and no signal is seen. In addition, if such pickup were present, then a signal in other magnetic configurations would have been present and it is not.

TABLE I. Fit parameters for the rise time of FC-FILD signals. The upper (c_{upper}) and lower (c_{lower}) 95% confidence intervals for the fit are shown. The coefficient has units of ms.

| Channel	c_{lower}	c_{fit}	c_{upper}
1	−10.6	3.3	17.2
2	2.47	4.28	6.09
3	0.868	2.42	3.98
4	1.46	2.99	4.52
5	2.43	3.42	4.41

While the temporal evolution and relative signal amplitude agree well with the notion that escaping fast ions were measured, absolute amplitudes disagree with simulations. From the diagnostic side, the measured signals were at the lower end of the measurable range (being 100 pA). However, these signals were still significant and clearly resolvable above the background signal fluctuations. Gyro center simulations with slowing down and pitch angle scattering were performed with the BEAMS3D code from NBI birth to the equilibrium last closed flux surface. These simulations were then continued in collisionless gyro-orbit mode from that point to the wall of W7-X. Markers that hit the diagnostic head (in its fully inserted position) were then followed backward in time for 60 μs, duplicated in order to fill the gyro-orbit, and then followed forward again to the diagnostic head. This helps improve statistics and allows fast computation of loads to the diagnostic head at different insertion depths. Figure 11 depicts the raw simulated signal to each finger of the detector for various insertion depths of the diagnostic. This simulation includes the full wall and detector geometry. Particles reaching the fingers are counted and used to construct a signal. No filtering by energy is performed in this analysis. The shadowing of the sensor using the detector head is discussed in the Appendix.
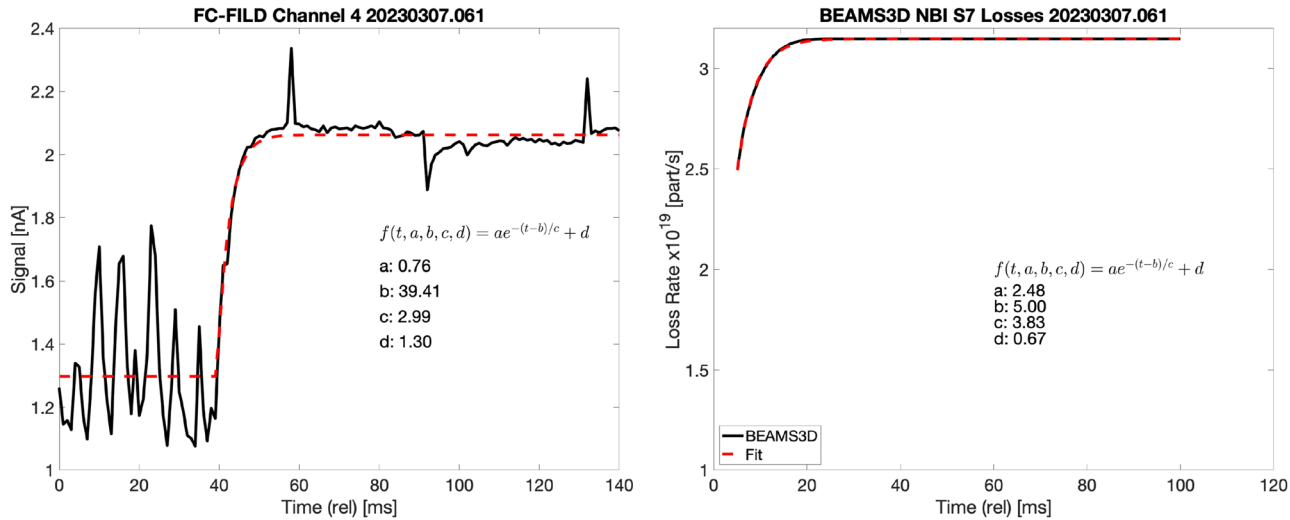
FIG. 10. Measured data (left) and simulation (right) for a single blip of source 7 for the W7-X neutral beam system. A fit curve is applied to both signals showing similar timescales for the rise in signal. Simulations data are for all particles lost through the equilibrium LCFS in the BEAMS3D simulation.
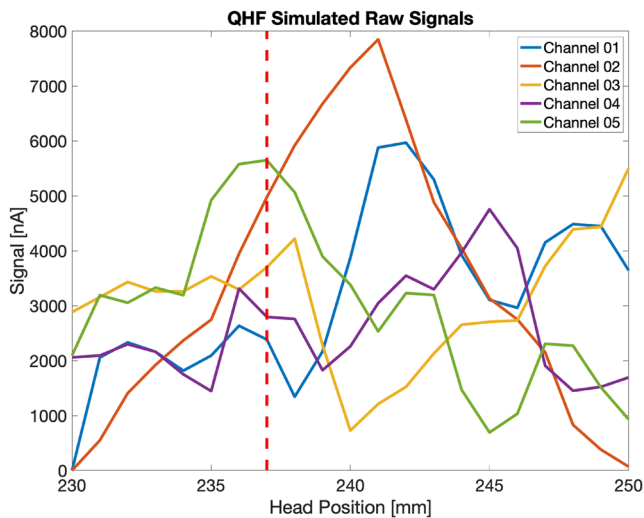
FIG. 11. Simulated detector response for different positions of the detector head with nominal position marked as a red dashed vertical line. The finger and detector geometry is considered in this analysis, but no filtering by energy has been performed.

The simulated amplitudes are in the μA range, whereas the measured signal is in the nA range. Attempting to account for the energy filtering of the FC-FILD detector itself reduces the simulated signal in all but channels 1 and 2 to zero. Four candidate effects may explain this apparent amplitude discrepancy. First, simulations neglect the presence of collisions and the edge electric field, which may be significant in W7-X, resulting in additional signal attenuation and pitch angle scattering. Second, simulations do not account for charge exchange, which could also significantly attenuate the signal. Third, our simulation workflow filters out some particles born just outside the edge of the plasma. These particles could contribute to signals arising from prompt losses, which would show up in the sensor fingers 3 and 4. Finally, the exact position of the detector head is unknown, and small variations in position can make a large difference in signal as seen in Fig. 11. Simulation results here should be viewed as an upper limit on signals for these reasons.

IV. CONCLUSIONS

The first measurements with the Faraday cup fast ion loss detector on W7-X have been made. The prototype diagnostic system demonstrates an in-wall-tile mounting concept for the sensors, allowing for future multi-point measurement of escaping fast ions. Such measurements are critical to the confirmation of improved fast ion confinement with plasma beta $(\beta = 2\mu_0 p/B^2)$, as single point measurements fail to capture changes in losses in stellarators. The measured signal is dominated by the 50 and 25 keV detector response, which is characteristic of the full and half energy components of the neutral beam injection system. A time dependent analysis of the measured signals confirms that they arise from lost fast ions and not changes in plasma parameters as the neutral beam is fired. A similar analysis of simulation data confirms that

the measured timescales are consistent with lost fast ions. Discrepancies between simulated and measured signal amplitudes can be attributed to missing physics in the simulations and limited experimental data. While these first measurements are promising, data acquisition was hampered by poor aperture design, which limited signal acquisition to a single magnetic configuration. Finally, the presence of a signal in channel 5 remains a mystery and is left for future analysis.

Figure 12 depicts a redesigned detector head front carbon tile setup, which is predicted to drastically improve the signal in more magnetic configurations. In this design, the sensor has been moved to the leading edge, where most fast ion losses are expected. More of the sensor itself is exposed through removal of carbon material on the front tile. This helps limit the self-shadowing effect of the detector head itself. It should be noted that while covered by the carbon tile, the electrical contacts are visible in the picture, and it is possible that some particles may reach them. In the simulation depicted, no particle reaches the sensor with the previous design. While these modifications are predicted to improve signal, being able to move the sensor to the surface of the carbon tile would further improve detector response. These modifications have been made and are awaiting testing in the next experimental campaign.

For future in-tile first wall mounting, the sensor should be moved as close to the surface of the tile as possible. This limits the shadowing effect and helps improve the signal. To achieve this, a small offset block of CuCrZr could be placed between the sensor and underlying heat sink. Modifications to the substrate could then be made so that electrical connections are made from the backside of the substrate. This would then avoid thin sections of carbon, which could be prone to cracking. Switching to tungsten tiles, one could also envision the sensor being directly deposited onto the tile itself, opening the possibility of the addition of many more channels.

The sensor itself will degrade over time due to two effects: sputtering and deposition. Physical sputtering of the insulating layers will degrade them over time, thinning them and biasing them toward lower energies. Meanwhile, deposition of material eroded elsewhere in the device will essentially thicken the insulating layer, biasing the detector toward higher energies. The W7-X device can serve as a
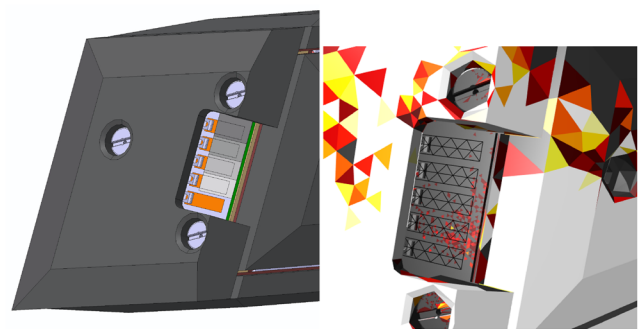
FIG. 12. CAD rendering (left) and BEAMS3D simulated loads (right) for the modified front showing improved access for particles to the sensor. In the CAD rendering, the orange color indicates aluminum fingers, while shades of gray indicate increasing aluminum oxide thickness. In the simulations (performed for the high mirror magnetic configuration), a black wire mesh is used to depict the fingers. Simulation colors indicate total marker strikes per triangle.

04 March 2025 08:16:00

testbed for understanding this effect, given its long-pulse nature. Here, calibration of the sensor in a tunable ion beam (as was done before) both before and after an operation campaign could help better assess this effect. Finally, we note that the effect of high neutron fluence on the sensor should be addressed in the future work.

ACKNOWLEDGMENTS

AUTHOR DECLARATIONS

Conflict of Interest

The authors have no conflicts to disclose.

Author Contributions

Samuel A. Lazerson: Conceptualization (lead); Data curation (lead); Formal analysis (lead); Funding acquisition (lead); Investigation (lead); Methodology (lead); Project administration (lead); Resources (lead); Software (lead); Supervision (lead); Validation (lead); Visualization (lead); Writing – original draft (lead); Writing – review & editing (equal). **David J. Kulla**: Data curation (equal); Formal analysis (equal); Investigation (equal); Software (equal); Writing – review & editing (equal). **Alexandra LeViness**: Data curation (equal); Formal analysis (equal); Investigation (equal); Writing – review & editing (equal). **Brandon F. Lee**: Data curation (equal); Formal analysis (equal); Investigation (equal); Writing – review & editing (equal). **Matthias Steffen**: Conceptualization (equal); Methodology (equal); Writing – review & editing (supporting). **Beate Kursinski**: Conceptualization (supporting); Methodology (equal); Project administration (equal); Writing – review & editing (supporting). **Karsten Ewert**: Methodology (supporting); Project administration (supporting); Resources (supporting); Validation (equal); Writing – review & editing (supporting).

DATA AVAILABILITY

Raw data were generated at the Wendelstein 7-X large scale facility. Derived data supporting the findings of this study are available from the corresponding author upon reasonable request.

APPENDIX: ORBIT MODELING

Simulations to demonstrate the self-shadowing of the detector head design were performed using the BEAMS3D code in collisionless gyro-orbit mode. Particles were initialized at the sensor face for a range of velocities scanning pitch angle and gyro-phase. These particles were followed backward considering the full detector geometry.
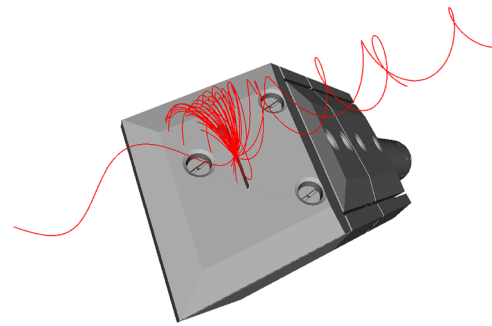
FIG. 13. BEAMS3D collisionless simulations of orbits through the aperture of the detector for the low shear magnetic configuration showing shadowing of the majority of orbits.

Figure 13 shows the orbits for these particles, the vast majority of which impacts the detector body. A few orbits are not shadowed by the detector body and can be traced backward in time into the plasma domain. This simulation was conducted for the low shear magnetic configuration, in which data were measured. Simulations for the standard and high mirror magnetic configurations show all orbits being shadowed. This helps explain the lack of signal in those magnetic configurations.

The large ratio between the number of particles that can make it into the detector slit and those that are shadowed can help explain the discrepancy between measured and simulated data. This is because simulations only considered particles that make it to the head and do not account for this shadowing. While the slit was included in the simulation, statistics are too low, given the small size of the aperture and even smaller percentage of particles that can make it to the sensor. This type of assessment must be made when considering future in-wall-tile style sensor installations.

REFERENCES

[1] D. S. Darrow, F. E. Cecil, V. Kiptily, K. Fullard, A. Horton, A. Murari, and JET EFDA Contributors, Rev. Sci. Instrum. **81**, 10D330 (2010).

[2] D. Jiménez-Rey, B. Zurro, J. Guasp, M. Liniers, A. Baciero, M. García-Muñoz, A. Fernández, G. García, L. Rodríguez-Barquero, and J. M. Fontdecaba, Rev. Sci. Instrum. **79**, 093511 (2008).

[3] A. Werner, A. Weller, D. S. Darrow, and the W7-AS Team, Rev. Sci. Instrum. **72**, 780 (2001).

[4] J. Galdon-Quiroga, M. Garcia-Munoz, M. Salewski, A. S. Jacobsen, L. Sanchis-Sanchez, M. Rodriguez-Ramos, J. Ayllon-Guerola, J. Garcia-Lopez, J. Gonzalez-Martin, M. C. Jimenez-Ramos, J. F. Rivero-Rodriguez, E. Viezzer, and the ASDEX Upgrade Team, Plasma Phys. Controlled Fusion **60**, 105005 (2018).

[5] S. Yamamoto, K. Ogawa, M. Isobe, D. S. Darrow, S. Kobayashi, K. Nagasaki, H. Okada, T. Minami, S. Kado, S. Ohshima, G. M. Weir, Y. Nakamura, S. Konoshima, N. Kemmochi, Y. Ohtani, and T. Mizuuchi, Rev. Sci. Instrum. **87**, 11D818 (2016).

[6] J. F. Rivero-Rodriguez, C. Perez Von Thun, M. Garcia-Muñoz, P. Beaumont, V. Kiptily, J. Garcia-Lopez, V. Goloborodko, M. C. Jimenez-Ramos, M. Rodriguez-Ramos, K. Schoepf, V. Yavorskij, and JET Contributors, Rev. Sci. Instrum. **92**, 043553 (2021).

[7] T. Klinger, T. Andreeva, S. Bozhenkov, C. Brandt, R. Burhenn, B. Buttenschön, G. Fuchert, B. Geiger, O. Grulke, H. Laqua, N. Pablant, K. Rahbarnia, T. Stange, A. von Stechow, N. Tamura, H. Thomsen, Y. Turkin, T. Wegner, I. Abramovic, S. Äkäslompolo, J. Alcuson, P. Aleynikov, K. Aleynikova, A. Ali, A. Alonso, G. Anda, E. Ascasibar, J. Bähner, S. Baek, M. Balden, J. Baldzuhn, M. Banduch, T.

Barbui, W. Behr, C. Beidler, A. Benndorf, C. Biedermann, W. Biel, B. Blackwell, E. Blanco, M. Blatzheim, S. Ballinger, T. Bluhm, D. Böckenhoff, B. Böswirth, L.-G. Böttger, M. Borchardt, V. Borsuk, J. Boscary, H.-S. Bosch, M. Beurskens, R. Brakel, H. Brand, T. Bräuer, H. Braune, S. Brezinsek, K.-J. Brunner, R. Bussiahn, V. Bykov, J. Cai, I. Calvo, B. Cannas, A. Cappa, A. Carls, D. Carralero, L. Carraro, B. Carvalho, F. Castejon, A. Charl, N. Chaudhary, D. Chauvin, F. Chernyshev, M. Cianciosa, R. Citarella, G. Claps, J. Coenen, M. Cole, M. Cole, F. Cordella, G. Cseh, A. Czarnecka, K. Czerski, M. Czerwinski, G. Czymek, A. da Molin, A. da Silva, H. Damm, A. de la Pena, S. Degenkolbe, C. Dhard, M. Dibon, A. Dinklage, T. Dittmar, M. Drevlak, P. Drewelow, P. Drews, F. Durodie, E. Edlund, P. van Eeten, F. Effenberg, G. Ehrke, S. Elgeti, M. Endler, E. Ennis, H. Esteban, T. Estrada, J. Fellinger, Y. Feng, E. Flom, H. Fernandes, W. Fietz, W. Figacz, J. Fontdecaba, O. Ford, T. Fornal, H. Frerichs, A. Freund, T. Funaba, A. Galkowski, G. Gantenbein, Y. Gao, J. García Regaña, D. Gates, J. Geiger, V. Giannella, A. Gogoleva, B. Goncalves, A. Goriaev, D. Gradic, M. Grahl, J. Green, H. Greuner, A. Grosman, H. Grote, M. Gruca, C. Guerard, P. Hacker, X. Han, J. Harris, D. Hartmann, D. Hathiramani, B. Hein, B. Heinemann, P. Helander, S. Henneberg, M. Henkel, J. Hernandez Sanchez, C. Hidalgo, M. Hirsch, K. Hollfeld, U. Höfel, A. Hölting, D. Höschen, M. Houry, J. Howard, X. Huang, Z. Huang, M. Hubeny, M. Huber, H. Hunger, K. Ida, T. Ilkei, S. Illy, B. Israeli, S. Jablonski, M. Jakubowski, J. Jelonnek, M. Jenzsch, T. Jesche, M. Jia, P. Junghanns, J. Kacmarczyk, J.-P. Kallmeyer, U. Kamionka, H. Kasahara, W. Kasparek, Y. Kazakov, N. Kenmochi, C. Killer, A. Kirschner, R. Kleiber, J. Knauer, M. Knaup, A. Knieps, T. Kobarg, G. Kocsis, F. Köchl, Y. Kolesnichenko, A. Könies, R. König, P. Kornejew, J.-P. Koschinsky, F. Köster, M. Krämer, R. Krampitz, A. Krämer-Flecken, N. Krawczyk, T. Kremeyer, J. Krom, M. Krychowiak, I. Ksiazek, M. Kubkowska, G. Kühner, T. Kurki-Suonio, P. Kurz, S. Kwak, M. Landreman, P. Lang, R. Lang, A. Langenberg, S. Langish, H. Laqua, R. Laube, S. Lazerson, C. Lechte, M. Lennartz, W. Leonhardt, C. Li, C. Li, Y. Li, Y. Liang, C. Linsmeier, S. Liu, J.-F. Lobsien, D. Loesser, J. Loizu Cisquella, J. Lore, A. Lorenz, M. Losert, A. Lücke, A. Lumsdaine, V. Lutsenko, H. Maaßberg, O. Marchuk, J. Matthew, S. Marsen, M. Marushchenko, S. Masuzaki, D. Maurer, M. Mayer, K. McCarthy, P. McNeely, A. Meier, D. Mellein, B. Mendelevitch, P. Mertens, D. Mikkelsen, A. Mishchenko, B. Missal, J. Mittelstaedt, T. Mizuuchi, A. Mollen, V. Moncada, T. Mönnich, T. Morisaki, D. Moseev, S. Murakami, G. Náfrádi, M. Nagel, D. Naujoks, H. Neilson, R. Neu, O. Neubauer, U. Neuner, T. Ngo, D. Nicolai, S. Nielsen, H. Niemann, T. Nishizawa, R. Nocentini, C. Nührenberg, J. Nührenberg, S. Obermayer, G. Offermanns, K. Ogawa, J. Ölmanns, J. Ongena, J. Oosterbeek, G. Orozco, M. Otte, L. Pacios Rodriguez, N. Panadero, N. Panadero Alvarez, D. Papenfuß, S. Paqay, E. Pasch, A. Pavone, E. Pawelec, T. Pedersen, G. Pelka, V. Perseo, B. Peterson, D. Pilopp, S. Pingel, F. Pisano, B. Plaum, G. Plunk, P. Pölöskei, M. Porkolab, J. Proll, M.-E. Puiatti, A. Puig Sitjes, F. Purps, M. Rack, S. Récsei, A. Reiman, F. Reimold, D. Reiter, F. Remppel, S. Renard, R. Riedl, J. Riemann, K. Risse, V. Rohde, H. Röhlinger, M. Romé, D. Rondeshagen, P. Rong, B. Roth, L. Rudischhauser, K. Rummel, T. Rummel, A. Runov, N. Rust, L. Ryc, S. Ryosuke, R. Sakamoto, M. Salewski, A. Samartsev, E. Sanchez, F. Sano, S. Satake, J. Schacht, G. Satheeswaran, F. Schauer, T. Scherer, J. Schilling, A. Schlaich, G. Schlisio, F. Schluck, K.-H. Schlüter, J. Schmitt, H. Schmitz, O. Schmitz, S. Schmuck, M. Schneider, W. Schneider, P. Scholz, R. Schrittwieser, M. Schröder, T. Schröder, R. Schroeder, H. Schumacher, B. Schweer, E. Scott, S. Sereda, B. Shanahan, M. Sibilia, P. Sinha, S. Sipliä, C. Slaby, M. Sleczka, H. Smith, W. Spiess, D. Spong, A. Spring, R. Stadler, M. Stejner, L. Stephey, U. Stridde, C. Suzuki, J. Svensson, V. Szabó, T. Szabolics, T. Szepesi, Z. Szökefalvi-Nagy, A. Tancetti, J. Terry, J. Thomas, M. Thumm, J. Travere, P. Traverso, J. Tretter, H. Trimino Mora, H. Tsuchiya, T. Tsujimura, S. Tulipán, B. Unterberg, I. Vakulchyk, S. Valet, L. Vano, B. van Milligen, A. van Vuuren, L. Vela, J.-L. Velasco, M. Vergote, M. Vervier, N. Vianello, H. Viebke, R. Vilbrandt, A. Vorköper, S. Wadle, F. Wagner, E. Wang, N. Wang, Z. Wang, F. Warmer, T. Wauters, L. Wegener, J. Weggen, Y. Wei, G. Weir, J. Wendorf, U. Wenzel, A. Werner, A. White, B. Wiegel, F. Wilde, T. Windisch, M. Winkler, A. Winter, V. Winters, S. Wolf, R. Wolf, A. Wright, G. Wurden, P. Xanthopoulos, H. Yamada, I. Yamada, R. Yasuhara, M. Yokoyama, M. Zanini, M. Zarnstorff, A. Zeitler, D. Zhang, H. Zhang, J. Zhu, M. Zilker, M. Zocco, S. Zoletnik, and M. Zuin, Nucl. Fusion **59**, 112004 (2019).

[8] D. Kulla, S. Lazerson, S. Günter, M. Hirsch, D. Hartmann, P. McNeely, N. Rust, and R. C. Wolf, Plasma Phys. Controlled Fusion **64**, 035006 (2022).

[9] M. Rodríguez-Ramos, M. Jiménez-Ramos, M. García-Muñoz, and J. García López, Nucl. Instrum. Methods Phys. Res., Sect. B **403**, 7 (2017).

[10] O. Putignano, E. Perelli Cippo, M. Rebai, G. Grosso, M. Nocente, M. Pillon, J. Ayllon-Guerola, and M. Garcia-Muñoz, Fusion Eng. Des. **173**, 112913 (2021).

[11] S. A. Lazerson, R. Ellis, C. Freeman, J. Ilagan, T. Wang, L. Shao, N. Allen, D. Gates, and H. Neilson, Rev. Sci. Instrum. **90**, 093504 (2019).

[12] D. Kulla, S. A. Lazerson, K. Hunger, H. Gerdes, and R. Bandorf, Rev. Sci. Instrum. **94**, 053503 (2023).

[13] G. Szalkowski, D. Darrow, and F. Cecil, Nucl. Instrum. Methods Phys. Res., Sect. A **848**, 87 (2017).

[14] M. Drevlak, J. Geiger, P. Helander, and Y. Turkin, Nucl. Fusion **54**, 073002 (2014).

[15] J. Faustin, W. Cooper, J. Graves, D. Pfefferlé, and J. Geiger, Nucl. Fusion **56**, 092006 (2016).

[16] S. Äkäslompolo, M. Drevlak, Y. Turkin, S. Bozhenkov, T. Jesche, J. Kontula, T. Kurki-Suonio, R. Wolf, and the W7-X Team, Nucl. Fusion **58**, 082010 (2018).

[17] S. A. Lazerson, O. Ford, S. Äkäslompolö, S. Bozhenkov, C. Slaby, L. Vanó, A. Spanier, P. McNeely, N. Rust, D. Hartmann, P. Poloskei, B. Buttenschon, R. Burhenn, N. Tamura, R. Bussiahn, T. Wegner, M. Drevlak, Y. Turkin, K. Ogawa, J. Knauer, K. J. Brunner, E. Pasch, M. Beurskens, H. Damm, G. Fuchert, P. Nelde, E. Scott, N. Pablant, A. Langenberg, P. Traverso, P. Valson, U. Hergenhahn, A. Pavone, K. Rahbarnia, T. Andreeva, J. Schilling, C. Brandt, U. Neuner, H. Thomsen, N. Chaudhary, U. Höefel, T. Stange, G. Weir, N. Marushchenko, M. Jakubowski, A. Ali, Y. Gao, H. Niemann, A. Puig Sitjes, S. Koenig, R. Schroeder, N. den Harder, B. Heinemann, C. Hopf, R. Riedl, R. C. Wolf, and the W7-X Team, Nucl. Fusion **61**, 096008 (2021).

[18] S. A. Lazerson, D. Pfefferlé, M. Drevlak, H. Smith, J. Geiger, S. Äkäslompolo, P. Xanthopoulos, A. Dinklage, O. Ford, P. McNeely, N. Rust, S. Bozhenkov, D. Hartmann, K. Rahbarnia, T. Andreeva, J. Schilling, C. Brandt, U. Neuner, H. Thomsen, R. C. Wolf, and the W7-X Team, Nucl. Fusion **61**, 096005 (2021).

[19] S. A. Lazerson, D. Kulla, D. A. Hartmann, P. McNeely, N. Rust, and the W7-X Team, Nucl. Fusion **63**, 096012 (2023).

[20] M. Machielsen, J. P. Graves, H. W. Patten, C. Slaby, and S. Lazerson, J. Plasma Phys. **89**, 955890202 (2023).

[21] S. A. Lazerson, J. Geiger, D. Kulla, A. LeViness, S. Bozhenkov, C. Killer, K. Ogawa, M. Isobe, P. McNeely, N. Rust, D. Hartmann, and the W7-X Team, Plasma Phys. Controlled Fusion **66**, 075017 (2024).

[22] S. A. Lazerson, D. Kulla, P. McNeely, N. Rust, L. van Ham, D. Hartmann, and the W7-X Team, Phys. Plasmas **31**, 072506 (2024).

[23] J. F. Ziegler, J. P. Biersack, and M. D. Ziegler, SRIM—The Stopping and Range of Ions in Matter, 15th ed. (SRIM Co., 2015).

[24] J. M. Faustin, W. A. Cooper, J. P. Graves, D. Pfefferlé, and J. Geiger, Plasma Phys. Controlled Fusion **58**, 074004 (2016).

[25] M. McMillan and S. A. Lazerson, Plasma Phys. Controlled Fusion **56**, 095019 (2014).

[26] S. Bannmann, O. Ford, U. Hoefel, A. Poloskei, A. Pavone, S. Kwak, J. Svensson, S. Lazerson, P. McNeely, N. Rust, D. Hartmann, E. Pasch, G. Fuchert, R. C. Wolf, and the W7-X-Team, J. Instrum. **18**(10), P10029 (2023).

[27] S. A. Lazerson, O. P. Ford, C. Nuehrenberg, S. Äkäslompolo, P. Z. Poloskei, M. Machielsen, P. McNeely, L. Vanó, N. Rust, S. Bozhenkov, T. W. Neelis, J. P. Graves, D. Pfefferlé, A. Spanier, D. Hartmann, N. Marushchenko, Y. Turkin, M. Hirsch, N. Chaudhary, U. Hoefel, T. Stange, G. Weir, N. Pablant, A. Langenberg, P. Traverso, P. Valson, J. Knauer, K. Jakob Brunner, E. Pasch, M. Beurskens, H. Damm, G. Fuchert, P. Nelde, E. Scott, U. Hergenhahn, A. Pavone, K. Rahbarnia, T. Andreeva, J. Schilling, C. Brandt, U. Neuner, H. Thomsen, M. Jakubowski, A. Ali, Y. Gao, H. Niemann, A. Puig Sitjes, R. Koenig, R. C. Wolf, and the W7-X Team, Nucl. Fusion **60**, 076020 (2020).